Supplementary materials for

Intrinsic high-strain-rate softening in a high-strength quenching and partitioning steel

C.P. Huang [a], M. Wang [a], K.Y. Zhu [b], Astrid Perlade [b], M.X. Huang [a*]

[a] Center for Structural Materials, Department of Mechanical Engineering, The University of Hong Kong, Pokfulam Road, Hong Kong, China

[b] ArcelorMittal Research, Voie Romaine-BP30320, 57583, Maizières-lès-Metz, France

*Corresponding author: Prof. M.X. Huang, email :mxhuang@hku.hk; Tel: +85228597906; Fax: +85228585415

Supplementary Note 1:

Calculations of austenite volume fraction and dislocation density

Based on the synchrotron XRD profiles, for all specimens, the austenite volume fraction and dislocation densities of both martensite and austenite were calculated. Using the initially undeformed specimen as an example, the detailed calculation procedures are illustrated as follows. Firstly, the measured synchrotron XRD profiles were fitted using the pseudo-Voigt function [1], as shown in Fig. S1. It can be seen that the residual (blue solid line) between the measured (black cross marks) and fitted (red solid line) profiles is very small, which indicating a good fitting.

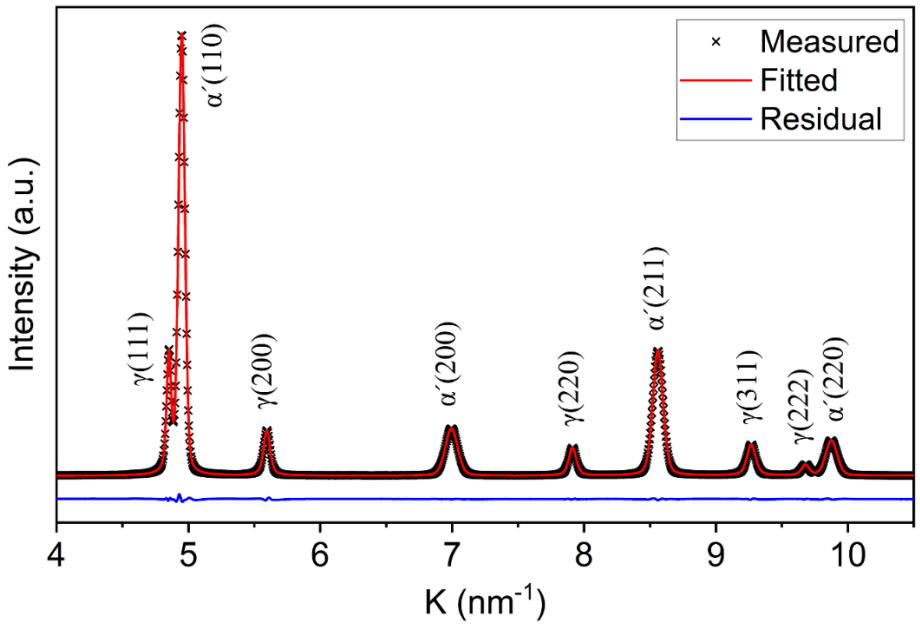

Fig. S1 The measured (black cross marks) and fitted (red solid line) synchrotron XRD profiles of the present Q&P sample at initially undeformed state. The residual between measured and fitted profiles is plotted in blue solid line.

Then, the austenite peaks including γ(111), γ(200), γ(220), γ(311), γ(222) and martensite peaks including α′(110), α′(200), α′(211), α′(220) shown in Fig. S1 were used for the calculation of volume fraction of austenite using the following equation, according to the ASTM E975 standard [2]:

$$V_\gamma = \frac{\frac{1}{n}\sum_{j=1}^{n}\frac{I_\gamma^j}{R_\gamma^j}}{\frac{1}{n}\sum_{j=1}^{n}\frac{I_\gamma^j}{R_\gamma^j}+\frac{1}{n}\sum_{j=1}^{n}\frac{I_\alpha^j}{R_\alpha^j}} \quad (1)$$

where *I* is the integrated intensity of each diffraction peak for each phase, and *n* is the number of diffraction peaks for each phase, *R* is the material scattering factor representing the theoretical intensity of each peak. For illustration, the values of material scattering factor *R* and integrated intensity of each peak *I* of the undeformed specimen is listed here inTable S1. Then, the volume fraction of austenite (γ) in the undeformed specimen is calculated to be 23.83%.

Using the above method, the austenite volume fractions of other interrupted specimens were calculated based on synchrotron XRD profiles.

Table S1 Values of *R* and *I* for each diffraction peak of undeformed specimen

Peak	γ(111)	γ(200)	γ(220)	γ(311)	γ(222)	α′(110)	α′(200)	α′(211)	α′(220)
R	1533.18	664.83	366.34	541.02	187.07	1955.49	251.01	549.50	163.81
I	1524.70	579.92	355.81	397.74	134.04	5649.62	604.51	1607.17	449.84

The dislocation densities of martensite and retained austenite were calculated by combination of modified Williamson-Hall (MWH) method and modified Warren-Averbach (MWA) method [3]. Using the calculation of dislocation density of martensite (α′) of the undeformed specimen as an example, four martensite peaks α′(110), α′(200), α′(211), α′(220) shown in Fig. S1 were extracted to calculate the dislocation density of martensite.

According to the MWH method, the diffraction peak broadening can be related to the dislocation density as follow:

$$\Delta K = 0.9/D + \pi A^2 b^2 \rho^{1/2} \, (K^2 \bar{C})/2 + O(K^4 \bar{C}^2) \tag{2}$$

where $K = 2\,sin\theta/\lambda$ is the reciprocal of the lattice spacing, and $\Delta K = 2cos\theta \, (\Delta\theta)/\lambda$ is the full width at half maximum (FWHM) of the corresponding peak plotted against *K*. θ is the Bragg diffraction angle, and λ is the wavelength of the synchrotron X-ray. *D* is the average size of the coherently scattering domains, which can be treated as the average crystallite size. *A* is a parameter that determined by the effective outer cut-off radius R_e of dislocations, *b* is the magnitude of Burgers vector, ρ is the average dislocation density. *O* represents the high-order terms of $K^2\bar{C}$ and can be neglected. $\bar{C}$ is the average dislocation contrast factor. For each $\{hkl\}$ reflection, the value of $\bar{C}$ can be given by [4]:

$$\bar{C} = \bar{C}_{h00}\left[1 - q\frac{h^2k^2 + k^2l^2 + h^2l^2}{(h^2 + k^2 + l^2)^2}\right] \tag{3}$$

where $\bar{C}_{h00}$ is the average dislocation contrast factor corresponding to the $\{h00\}$ reflection, q is a parameter indicating the fractions of edge and screw dislocations. Both $\bar{C}_{h00}$ and q values depend on the anisotropic elastic constants c_{11}, c_{12}, c_{44} and the dislocation types of the material. According to Equation (2), assuming the parameter A is a constant, then the values of D, ρ, and q are determined by the best linear fitting ΔK against $K^2\bar{C}$ obtained by the method of least squares, as shown by the MWH plot inFig. S2(a). However, the assumption of parameter A as a constant may introduce errors, especially for materials with high dislocation density, such as martensitic steel [5]. A is related to effective outer cut-off radius R_e of dislocations, which depends on the arrangement of dislocations, such as randomly distributed dislocation structure and dislocation cell structure [6]. It is noted that the R_e value can only be estimated from the tails of the diffraction line profile [7]. Therefore, in order to obtain more accurate dislocation density that account for the dislocation arrangement, a further Fourier analysis of the line profile using the MWA equation is required, and described as follow [8]:

$$lnA(L) \cong lnA^s(L) + Y(L)(K^2\bar{C}) + O'(K^4\bar{C}^2) \quad (4)$$

$$Y(L) = -(\rho\pi b^2 L^2/2)ln(R_e/L) \quad (5)$$

where L is the Fourier length, $A(L)$ is the real part of the Fourier coefficient of the $\{hkl\}$ diffraction peak, and can be simply obtained by Fourier transformation. $A^s(L)$ is the size contribution of the Fourier coefficient, O' is the negligible high-order term. According to Equation (4), the first-order coefficient $Y(L)$ can be obtained by fitting $lnA(L)$, with L fixed, against $K^2\bar{C}$, as shown by the MWA plot i nFig. S2(b). Then, Equation (5) leads to the following equation:

$$Y(L)/L^2 = (\pi b^2\rho/2)lnL - (\pi b^2\rho/2)lnR_e \quad (6)$$

The dislocation density ρ and effective outer cut-off radius R_e can be calculated from the slope term $\pi b^2\rho/2$ and intercept term $-(\pi b^2\rho/2)lnR_e$, respectively, from the linear fitting $Y(L)/L^2$ against lnL.

Finally, the dislocation density of martensite (α′) of the undeformed specimen is calculated to be 1.64×10^{15} m^{-2}. This value is in good agreement with previously reported martensite dislocation density of approximate 4.0×10^{15} m^{-2} in a Fe-0.22C (wt.%) quenched and tempered martensitic steel [9].

Using the above method, the dislocation densities of martensite (α′) and austenite (γ) of all specimens were calculated based on synchrotron XRD profiles.

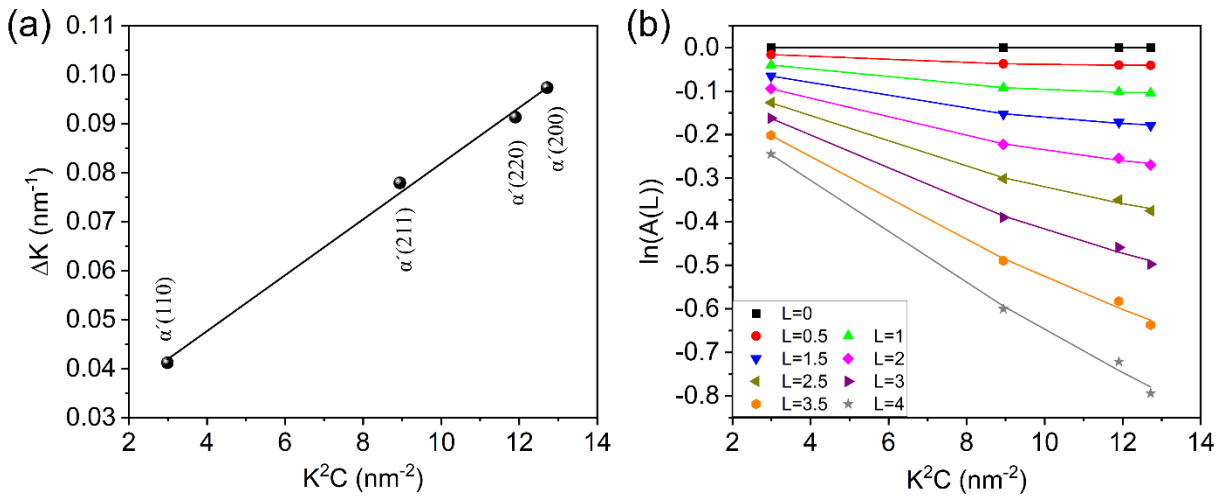

Fig. S2 (a) Modified Williamson-Hall plot and (b) Modified Warren-Averbach plot obtained from the diffraction peaks of martensite (α′) of the undeformed specimen.

Supplementary Note 2:

Effect of temperature rise due to adiabatic heating during high strain rates

The value of temperature rise ΔT resulting from the adiabatic heating during high-strain-rate deformation was calculated by the following equation [10]:

$$\Delta T = \frac{\beta \int_0^{\varepsilon} \sigma d\varepsilon}{\rho C_V} \tag{7}$$

where σ is the true stress, ε is the true strain, $\rho = 7.85 \times 10^3 kg \cdot m^{-3}$ is the steel density, $C_V = 485 J \cdot kg^{-1} \cdot K^{-1}$ is the specific heat capacity at constant volume for the steel [11]. β is the Taylor-Quinney factor of the steel that indicates the fraction of deformation energy converted into heat. Here we take $\beta = 0.8$ referring to the value of commercial 1020 steel [10].

According to equation (7), the temperature values ΔT during deformation at RT, 600 s^{-1} and 100 °C, 600 s^{-1} are plotted in Fig. S3. It can be seen that the highest temperature rise is ~28.4 °C at 10% true strain during deformation at RT, 600 s^{-1} (Fig. S3(a)) and ~20.1°C at 7.7% true strain during deformation at 100 °C, 600 s^{-1} (Fig. S3(b)).

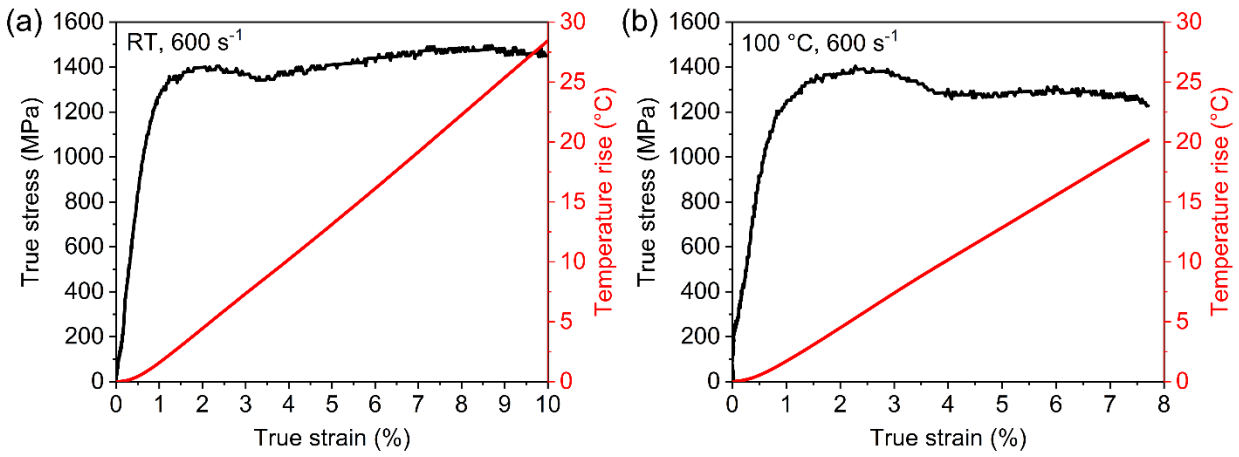

Fig. S3 True stress-strain curve (black curve) and temperature rise with true strain (red curve) of the present Q&P steel deformed at (a) RT, 600 s^{-1} and (b) 100 °C, 600 s^{-1}.

To further illustrate the possible effect of temperature rise on the mechanical behavior of the present Q&P steel due to adiabatic heating during high-strain-rate deformation, we additionally conducted tensile tests with temperature rise under quasi-static condition using the Linseis dilatometer L78, to simulate the temperature rise scenario under high-strain-rate deformati on.Fig. S4 shows the true stress-strain curves and temperature profiles of the present Q&P steel deformed under 10^{-3} s^{-1} at constant 27 °C (RT) and from initial 27 °C (RT) rising to 57 °C at 10% true strain. It is noticed that the true stress-strain curves are almost unchanged with temperature rise during deformation, suggesting that the temperature rise during high-strain-rate deformation at 27 °C (RT) would not affect the mechanical behavior of the present Q&P steel and thus could be neglected in this work.

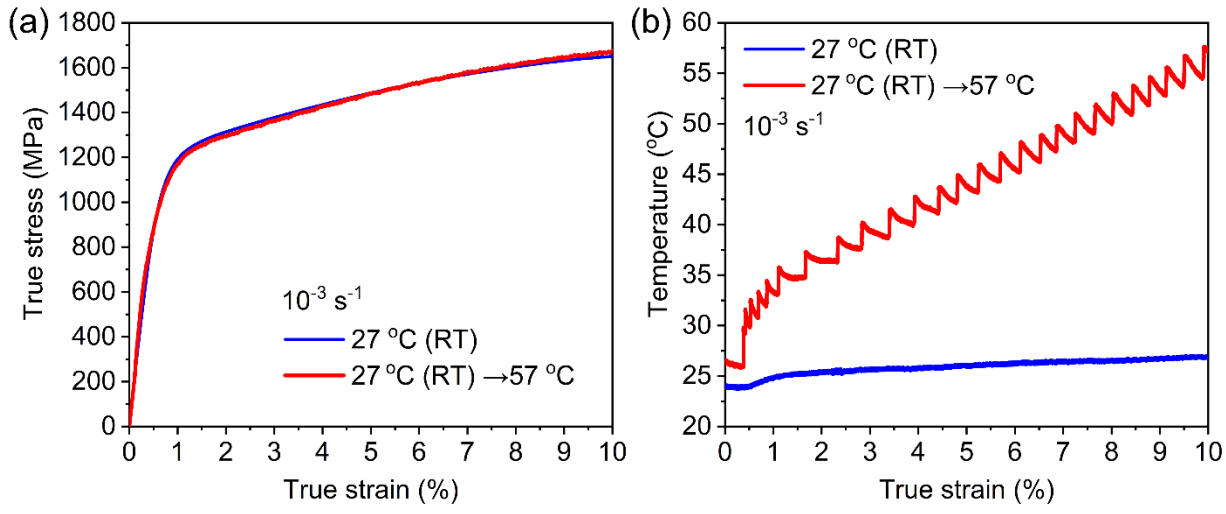

Fig. S4 (a) True stress-strain curves and (b) temperature profiles with true strain of the present Q&P steel deformed under 10^{-3} s^{-1} at constant 27 °C (RT) and from 27 °C (RT) to 57 °C. Note that the serrations of the temperature profiles were due to the precise temperature control by the inducting coils in the Linseis dilatometer L78.

Fig. S5 shows the true stress-strain curves and temperature profiles of the present Q&P steel deformed under 10^{-3} s^{-1} at constant 100 °C and from initial 100 °C rising to 125 °C at 10% true strain. It is noticed that the true stress-strain curve with temperature rise during deformation almost coincide with the true stress-strain curve with no temperature rise. This indicates that the temperature rise resulting from adiabatic heating during high-strain-rate deformation at 100 °C has neglectable effect on the mechanical behavior of the present Q&P steel.

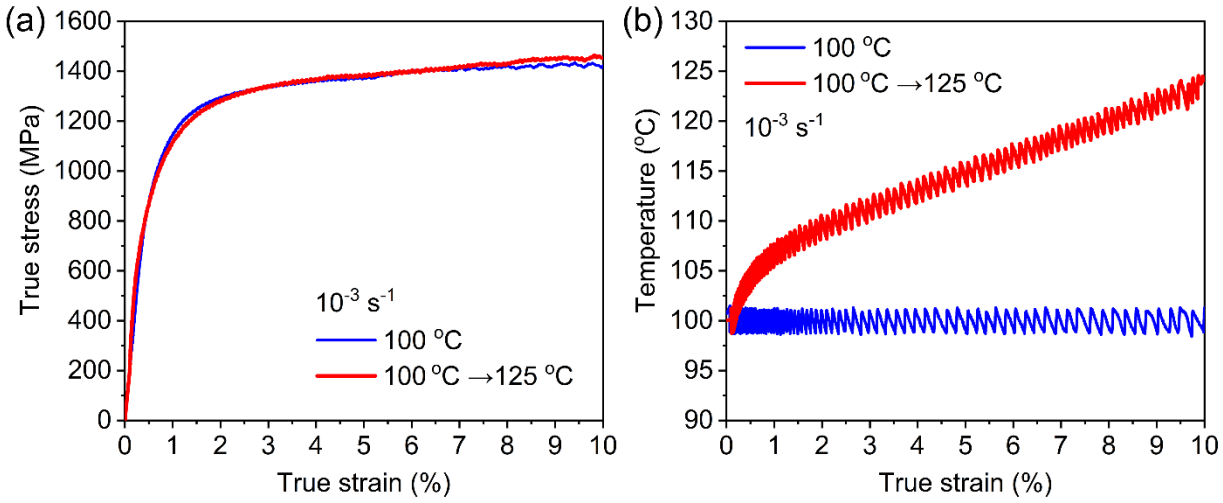

Fig. S5 (a) True stress-strain curves and (b) temperature profiles with true strain of the present Q&P steel deformed under 10^{-3} s^{-1} at constant 100 °C and from 100 °C to 125 °C. Note that the serrations of the temperature profiles were due to the precise temperature control by the inducting coils in the Linseis dilatometer L78.

Fig. S6 shows the true stress-strain curves of the present Q&P steel deformed under 10^{-3} s^{-1} at constant 100 °C, 200 °C, 250 °C, and 300 °C. The results indicate that tensile tests at 100 °C, 200 °C and 250 °C would not cause softening. The softening caused by elevated temperature occurs when the temperature is above ~300 °C.

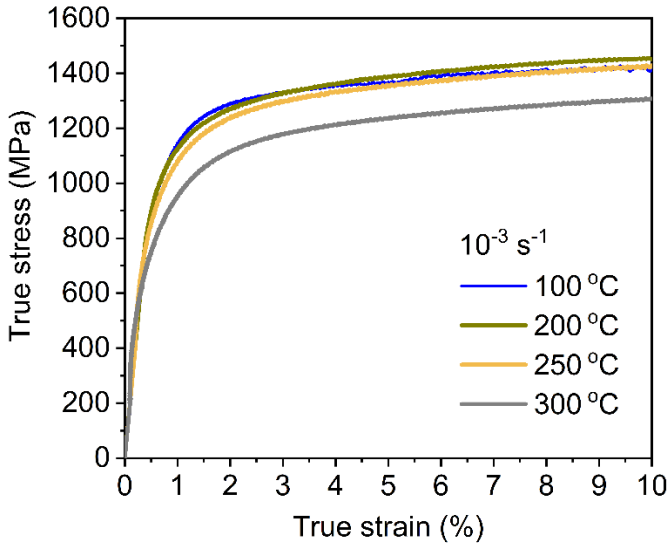

Fig. S6 True stress-strain curves of the present Q&P steel deformed under 10^{-3} s^{-1} at constant 100 °C, 200 °C, 250 °C, and 300 °C.

Supplementary Note 3:

Calculation of diffusion time t_d and waiting time t_w

In general, the interstitial carbon atoms would diffuse to dislocations, forming the Cottrell atmospheres. The diffusion time t_d is related to the diffusion radius r and diffusivity D by [12]:

$$t_d = \frac{r^2}{4D} = \frac{n_p v_a}{4\pi d_a c_p D_0 \exp\left(-Q/RT\right)} \tag{1}$$

where $r = \sqrt{n_p v_a / \pi d_a c_p}$ is the diffusion radius, n_p represents the number of pinning carbon atoms per atom along the dislocation line, v_a = 0.0117 nm^3 is the volume of iron atom in BCC martensite, d_a = 0.2546 nm is the diameter of iron atom, c_p = 0.65% is the atomic concentration of carbon in martensite matrix. Here we assume n_p = 1, the diffusion radius is then estimated to be r = 1.5 nm. $D = D_0 \exp\left(-Q/RT\right)$ is the diffusivity, Q = 66.9 $kJ \cdot mol^{-1}$ is the activation energy for carbon diffusion in martensite, D_0 = 0.02 $cm^2 \cdot s^{-1}$ is a pre-exponential factor [13], R = 8.314 $J \cdot K^{-1} \cdot mol^{-1}$ is the ideal gas constant, T is the absolute temperature. Hence, the diffusion time is estimated to be t_d = 6.57×10^{-4} s at 100 °C.

The waiting time t_w for temporarily pinned dislocations to break away is inversely proportional to plastic strain rate $\dot{\varepsilon}$ as [14,15]:

$$t_w = \frac{\Omega}{\dot{\varepsilon}} = \frac{b\rho_m\rho_f^{-1/2}}{\dot{\varepsilon}} \tag{2}$$

where ρ_m is the mobile dislocation density, ρ_f is the forest dislocation density, b = 0.2482 nm is the Burgers vector. Ω is the elementary incremental strain described by $\Omega = b\rho_m\rho_f^{-1/2}$. For the initial microstructure, the forest dislocation density was estimated to be ρ_f = 1.64×10^{15} m^{-2} according to the synchrotron XRD result. Assuming the ratio of mobile dislocation to forest dislocation density to be 18% for martensite matrix [16], the mobile dislocation density is estimated to be ρ_m = 2.95×10^{14} m^{-2}. The elementary incremental strain is estimated to be Ω = 1.81×10^{-3}, which is in good agreement with previous studies [14]. Hence, the waiting times (t_w) for loading at strain rates of 10^{-3} s^{-1} and 600 s^{-1} are 1.81 s and 3×10^{-6} s, respectively.

Fig. S7 plots the evolution of diffusion time t_d and waiting time t_w with the strain rate. It is obvious that $t_d < t_w$ when loading at 10^{-3} s^{-1} at 100 °C, and $t_d > t_w$ when loading at 600 s^{-1} at 100 °C.

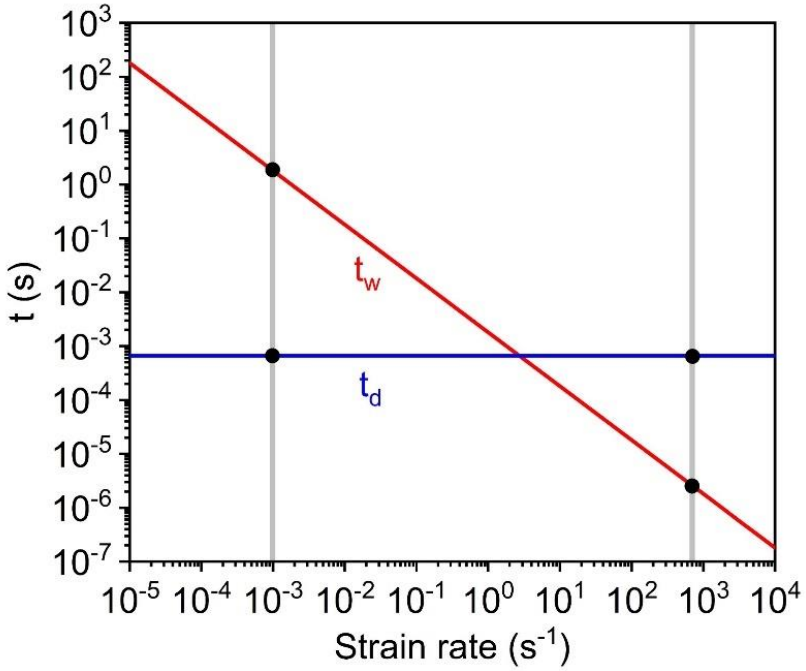

Fig. S7 Comparison of waiting time t_w and diffusion time t_d at 10^{-3} s^{-1} and 600 s^{-1} at 100 °C.

Supplementary Note 4:

Calculation of strengthening contributions of different mechanisms to the flow stress at 6%

To quantitatively analyze the various strengthening mechanisms at different loading conditions, the flow stress (σ) is decomposed into several terms as:

$$\sigma = \sigma_{fri} + \sigma_{ss} + \sigma_{gb} + \sigma_{dis} + \sigma_{drag} \quad (3)$$

where σ_{fri} is the strengthening of lattice friction, σ_{ss} is the strengthening of solid solution, σ_{gb} is the strengthening of grain boundary, σ_{dis} is the strengthening of dislocation forest, σ_{drag} is the strengthening of Cottrell drag force due to carbon-dislocation interaction.

The lattice friction σ_{fri} of pure iron at quasi-static deformation (10^{-3} s^{-1}) due to the Peierls barrier is well documented in literatures as ~ 50-100 MPa [17,18]. For the present Q&P steel under deformation at 10^{-3} s^{-1}, we take σ_{fri} = 80 MPa for estimation here. [17]. When the strain rate changes, the thermally activated gliding behavior of dislocations would change, which can be well described by the Arrhenius equation [19,20]: $\dot{\varepsilon} = \frac{\rho_m b d \nu}{M} exp\left(-\frac{\Delta G_0 - \sigma_{eff} V/M}{kT}\right)$, where ρ_m is the mobile dislocation density, b is the magnitude of Burgers vector, d is the average obstacle distance, ν is the attempt frequency, M is the Taylor factor, ΔG_0 is the Helmholtz free energy (activation energy), V is the activation volume, k is the Boltzmann constant, T is the absolute temperature, $\dot{\varepsilon}$ is the strain rate, σ_{eff} is the effective normal stress. The Arrhenius equation thus can be further converted as: $\sigma_{eff} = Kln\dot{\varepsilon} + B$, where $K = \frac{MkT}{V}$, and $B = \frac{M}{V}\left(\Delta G_0 - kTln\frac{\rho_m b d \nu}{M}\right)$. It is clear that σ_{eff} is a linear function of $ln\dot{\varepsilon}$ for the thermally activated glide of dislocations. For pure iron, when the deformation strain rate increases from 10^{-3} s^{-1} to 600 s^{-1}, the increment of effective stress σ_{eff} is well documented in literatures as ~100 MPa [21,22]. It should be noted that the increment of effective stress σ_{eff} of pure iron rising strain rate is totally caused by the increment of lattice friction σ_{fri}. Thus, for the present Q&P steel with similar body-centred cubic (BCC) lattice structure as pure iron, the increment of lattice friction σ_{fri} is also taken as approximate 100 MPa, when the deformation strain rate increases from 10^{-3} s^{-1} to 600 s^{-1}. Hence, the lattice friction σ_{fri} under deformation at 600 s^{-1} is taken as σ_{fri} = 180 MPa for estimation here.

The solid solution strengthening σ_{ss} is due to the short-range internal stresses produced by

elements in solid solution. Since most of carbon atoms are segregated to dislocations to form Cottrell atmospheres, it can be considered that the content of solute carbon atoms is negligibly small, and the corresponding solid solution strengthening can be neglected. Therefore, σ_{ss} in the present Q&P steel can be estimated by considering only the effect of substitutional solutes (i.e. Mn and Al), using a regression expression [23,24]: $\sigma_{ss} = 32X_{Mn} + 70X_{Al}$, where X denotes the weight concentration of individual elements marked in the subscript. Since the concentrations of Mn and Al are 9.3 wt.% and 2.0 wt.%, respectively, the solid solution strengthening is estimated to be σ_{ss} = 437 MPa. The solid solution strengthening σ_{ss} is independent of strain rate.

The grain boundary strengthening σ_{gb} can be described by the Hall-Petch relation as $\sigma_{gb} = k_{HP}d^{-1/2}$, where k_{HP} is the Hall-Petch parameter, d is the effective grain size. For the present Q&P steel, the Hall-Petch parameter k_{HP} is taken as 210 MPa·m$^{1/2}$ [25], and the effective grain size is considered to be the block size d = 1.1 um [26], which can be determined from the EBSD map. Thus, the grain boundary strengthening is estimated to be σ_{gb} = 201 MPa. The grain boundary strengthening σ_{gb} is independent of strain rate.

The dislocation forest strengthening σ_{dis} for polycrystalline materials is correlated to the dislocation density by the Taylor equation as [19]:

$$\sigma_{dislocation} = M\alpha\mu b\sqrt{\rho} \tag{4}$$

where M = 2.7 is the average Taylor factor [27], α = 0.2 is a dimensionless constant reflecting the interaction strength between forest dislocations [28], μ = 80 GPa is the shear modulus of martensite matrix, b = 0.2482 nm is the magnitude of Burgers vector of martensite matrix, and ρ is the dislocation density. For simplification, here we only use the dislocation density of martensite matrix to estimate the forest dislocation strengthening of the present Q&P steel. The strengthening of the dislocation forest can be estimated according to the dislocation density calculated from the synchrotron XRD data. For instance, the dislocation density of martensite matrix at 6% strain is ρ = 1.83×10^{15} m^{-2}, thus the dislocation strengthening to the flow stress at 6% is estimated to be $\sigma_{dislocation}$ = 458 MPa. The dislocation forest strengthening σ_{dis} is independent of strain rate.

The Cottrell drag force F_{drag} of dislocations due to the carbon atmospheres surrounding

dislocations is approximately given by [29]:

$$F_{drag} = \frac{\pi c_0 D A^2}{\Omega b^2 k T v} \tag{5}$$

where c_0 = 0.18% is the atomic concentration of carbon at infinite distance from the dislocation, D is the diffusion coefficient of carbon atoms, b = 0.2482 nm is the magnitude of Burgers vector, $k = 1.38\times10^{-23}$ J·K^{-1} is the Boltzmann constant, T is the absolute temperature, v is the dislocation velocity. A is the interaction parameter between dislocations and carbon atoms due to a size misfit, determined by $A=(1+\nu)\mu b\Omega\delta/[\pi(1-\nu)]$. Here, $\Omega = 4\pi r^3/3$ is the atomic volume of the interstitial carbon atom. r = 0.07 nm is the radius of carbon atom. ν = 0.3 is the Poisson ratio, μ = 80 GPa is the shear modulus, δ is the size misfit parameter, and approximately equal to 0.2 for carbon atom in the interstitial site of BCC iron [30]. The dislocation velocity v is correlated to the macroscopic plastic strain rate $\dot{\varepsilon}$ by Orowan equation [31] as $\dot{\varepsilon} = \rho_m b v / M$. Here, $\rho_m \approx 0.18\rho$ is the mobile dislocation density, M is the average Taylor factor. The stress contributed by the Cottrell drag force is $\sigma_{drag} = M\tau_{drag} = MF_{drag}/b$. Thus, the strengthening from Cottrell drag force σ_{drag} can be related to the mobile dislocation density ρ_m and plastic strain rate $\dot{\varepsilon}$ as:

$$\sigma_{drag} = \frac{\pi c_0 D A^2 \rho_m}{\Omega b^2 k T \dot{\varepsilon}} \tag{6}$$

Thus, when loading at 10^{-3} s^{-1} at 100 °C, the strengthening contribution of Cottrell drag force is estimated to be σ_{drag} = 208 MPa. When loading at 600 s^{-1} at 100 °C, the strengthening contribution of Cottrell drag force is estimated to be σ_{drag} = 3.47×10^{-4} MPa, which is too small and could be neglected.

Fig. S8 plots the contributions of different strengthening mechanisms to the flow stress at 6% under different loading conditions. In comparison to the continuous deformation at quasi-static strain rate, for the continuous high-strain-rate deformation, the lattice friction increased ~100 MPa, whereas the Cottrell drag force decreased ~208 MPa. Thus, the overall flow stress decreased ~108 MPa. For the interrupted high-strain-rate load-unload-load test, the increment of lattice friction and Cottrell drag force both exist, thus exhibits the highest flow stress.

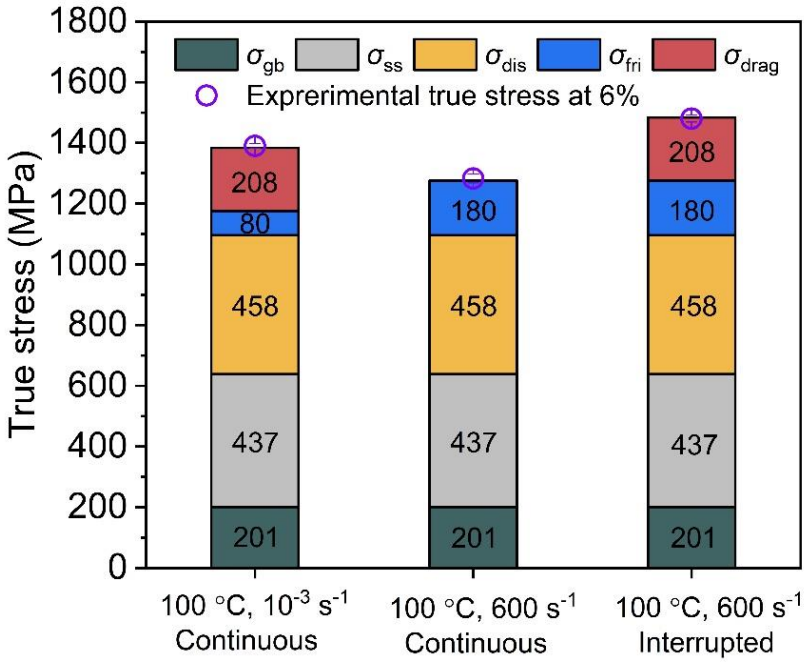

Fig. S8 Contributions of different strengthening mechanisms to the flow stress at 6% under different loading conditions

References:

[1] De Keijser TH, Langford J, Mittemeijer EJ, et al. Use of the Voigt function in a single-line method for the analysis of X-ray diffraction line broadening. Journal of Applied Crystallography. 1982;15(3):308-314.

[2] Standard A. E975-03: Standard practice for x-ray determination of retained austenite in steel with near random crystallographic orientation. ASTM, West Conshohocken, PA. 2003.

[3] Ungár T, Ott S, Sanders P, et al. Dislocations, grain size and planar faults in nanostructured copper determined by high resolution X-ray diffraction and a new procedure of peak profile analysis. Acta materialia. 1998;46(10):3693-3699.

[4] Dragomir I, Ungár T. The dislocations contrast factors of cubic crystals in the Zener constant range between zero and unity. Powder Diffraction. 2002;17(2):104-111.

[5] Akama D, Tsuchiyama T, Takaki S. Change in Dislocation Characteristics with Cold Working in Ultralow-carbon Martensitic Steel. ISIJ International. 2016;56(9):1675-1680.

[6] Takebayashi S, Kunieda T, Yoshinaga N, et al. Comparison of the dislocation density in martensitic steels evaluated by some X-ray diffraction methods. ISIJ international. 2010;50(6):875-882.

[7] Ungár T, Groma I, Wilkens M. Asymmetric X-ray line broadening of plastically deformed crystals. II. Evaluation procedure and application to [001]-Cu crystals. Journal of applied crystallography. 1989;22(1):26-34.

[8] Ungár T, Gubicza J, Ribárik G, et al. Crystallite size distribution and dislocation structure determined by diffraction profile analysis: principles and practical application to cubic and hexagonal crystals. Journal of applied crystallography. 2001;34(3):298-310.

[9] Harjo S, Kawasaki T, Tomota Y, et al. Work Hardening, Dislocation structure, and load partitioning in lath martensite determined by in situ neutron diffraction line profile analysis. Metallurgical and Materials Transactions A. 2017;48(9):4080-4092.

[10] Rittel D, Zhang L, Osovski S. The dependence of the Taylor–Quinney coefficient on the dynamic loading mode. Journal of the Mechanics and Physics of Solids. 2017;107:96-114.

[11] Zou D, Li S, He J. Temperature and strain rate dependent deformation induced martensitic transformation and flow behavior of quenching and partitioning steels. Materials Science and Engineering: A. 2017;680:54-63.

[12] Mola J, Luan G, Huang Q, et al. Dynamic strain aging mechanisms in a metastable austenitic stainless steel. Acta Materialia. 2021;212:116888.

[13] Thomas G, Speer J, Matlock D. Quenched and partitioned microstructures produced via Gleeble simulations of hot-strip mill cooling practices. Metallurgical and Materials Transactions A. 2011;42(12):3652-3659.

[14] Kubin L, Estrin Y. Evolution of dislocation densities and the critical conditions for the Portevin-Le Chatelier effect. Acta metallurgica et materialia. 1990;38(5):697-708.

[15] Kubin L, Estrin Y. The Critical Conditions for Jerky Flow. Discussion and Application to Cu Mn Solid Solutions. Physica status solidi (b). 1992;172(1):173-185.

[16] Hatem T, Zikry M. A model for determining initial dislocation-densities associated with martensitic transformations. Materials Science and Technology. 2011;27(10):1570-1573.

[17] Gutiérrez I, Altuna M. Work-hardening of ferrite and microstructure-based modelling of its mechanical behaviour under tension. Acta materialia. 2008;56(17):4682-4690.

[18] Lee S, Estrin Y, De Cooman BC. Constitutive modeling of the mechanical properties of V-added medium manganese TRIP steel. Metallurgical and Materials Transactions A. 2013;44(7):3136-3146.

[19] Mecking H, Kocks U. Kinetics of flow and strain-hardening. Acta metallurgica. 1981;29(11):1865-1875.

[20] Li Y, Luo Z, Liang Z, et al. Effect of carbon on strain-rate and temperature sensitivity of twinning-induced plasticity steels: modeling and experiments. Acta Materialia. 2019;165:278-293.

[21] Ostwaldt D, Klepaczko J, Klimanek P. Compression tests of polycrystalline α-iron up to high strains over a large range of strain rates. Le Journal de Physique IV. 1997;7(C3):C3-385-C3-390.

[22] Muller T. High strain rate behaviour of iron and nickel. Journal of Mechanical Engineering Science. 1972;14(3):161-167.

[23] Sohn S, Lee B-J, Lee S, et al. Effects of aluminum content on cracking phenomenon occurring during cold rolling of three ferrite-based lightweight steel. Acta materialia. 2013;61(15):5626-5635.

[24] Li Y, Zhao S, He S, et al. Enhancing yield stress and uniform elongation in an ultrathin packaging steel via controlling dislocation density. International Journal of Plasticity. 2022:103334.

[25] Kamikawa N, Sato K, Miyamoto G, et al. Stress–strain behavior of ferrite and bainite with nano-precipitation in low carbon steels. Acta Materialia. 2015;83:383-396.

[26] Morito S, Yoshida H, Maki T, et al. Effect of block size on the strength of lath martensite in low carbon steels. Materials Science and Engineering: A. 2006;438:237-240.

[27] He BB, Hu B, Yen HW, et al. High dislocation density–induced large ductility in deformed and partitioned steels. Science. 2017;357(6355):1029-1032.

[28] Mughrabi H. The α-factor in the Taylor flow-stress law in monotonic, cyclic and quasi-stationary deformations: Dependence on slip mode, dislocation arrangement and density. Current Opinion in Solid State and Materials Science. 2016;20(6):411-420.

[29] Takeuchi S, Argon AS. Glide and climb resistance to the motion of an edge dislocation due to dragging a Cottrell atmosphere. Philosophical Magazine A. 1979;40(1):65-75.

[30] Hull D, Bacon DJ. Introduction to dislocations. Butterworth-Heinemann; 2001.

[31] Qin Y, Greaney PA, Evans TM, et al. A critical dislocation velocity for serration mechanism transition in a nickel-chromium solid solution alloy. International Journal of Plasticity. 2021;145:103071.